Solar RRL

RESEARCH ARTICLE OPEN ACCESS

Suppressing Molecular Aggregation Enables Efficient and Thermally Stable Ternary Bilayer Organic Solar Cells

Woojin Lee[1] | Hye Won Cho[1] | Tack Ho Lee[2] | Dongchan Lee[3] | Yung Jin Yoon[1] | Sujung Park[3] | Shinuk Cho[3] | Jin Young Kim[1,4] | Song Yi Park[5]

[1]School of Energy and Chemical Engineering, Ulsan National Institute of Science and Technology (UNIST), Ulsan, Republic of Korea | [2]Graduate Department of Chemical Materials, Institute for Plastic Information and Energy Materials, Sustainable Utilization of Photovoltaic Energy Research Center, Pusan National University, Busan, Republic of Korea | [3]Department of Semiconductor Physics & Engineering and Energy Harvest Storage Research Center, University of Ulsan, Ulsan, Republic of Korea | [4]Graduate School of Carbon Neutrality, Ulsan National Institute of Science and Technology (UNIST), Ulsan, Republic of Korea | [5]Department of Physics, Pukyong National University, Busan, Republic of Korea

Correspondence: Jin Young Kim (jykim@unist.ac.kr) | Song Yi Park (songyi@pknu.ac.kr)

Received: 5 January 2026 | **Revised:** 3 February 2026 | **Accepted:** 25 February 2026

Keywords: bilayer organic solar cells | non-fullerene acceptors | ternary organic solar cells | thermal stability

ABSTRACT

Bilayer organic solar cells (OSCs) have been actively investigated due to more ideal photoactive layer structures and possibly better device stability compared to those of bulk-heterojunction OSCs. Here, we introduce a binary non-fullerene acceptor layer composed of IDIC and IT-4F into bilayer OSCs and investigate its effects on device performance and thermal stability. We found that IT-4F suppresses IDIC aggregation, which provides ideal interface morphologies between acceptor and electron transport layers, resulting in improved power conversion efficiency. In addition, due to suppressed IDIC aggregation, PM6/IDIC:IT-4F films showed robust thermal durability upon various pre-annealing test conditions. Moreover, PM6/IDIC:IT-4F bilayer OSCs exhibited improved stability compared to that of PM6/IDIC devices under continuous thermal annealing conditions. Whereas all photovoltaic parameters deteriorated upon thermal annealing in PM6/IDIC devices, only open-circuit voltages were reduced in PM6/IDIC:IT-4F devices, possibly due to a minor aggregation of IDIC. Nevertheless, binary acceptor layer reduced non-radiative voltage losses in bilayer OSCs, suggesting that there is more room to achieve better device stability by proper material selection. This work demonstrates that introducing a binary acceptor layer into bilayer OSCs can be an effective strategy to achieve both high efficiency and improved stability, especially when the given NFA tends to aggregate strongly.

1 | Introduction

Developing novel non-fullerene acceptors (NFAs) and conjugated polymer donors has enabled organic solar cells (OSCs) to achieve power conversion efficiency (PCE) over 20% [1–3]. Such exceptional progress has opened up the possibility of commercializing OSCs, owing to their unique advantages such as mechanical flexibility, light weight, and the facile fabrication of large-area devices via roll-to-roll and solution processing [4, 5]. However, since organic semiconductors generally exhibit short exciton diffusion lengths and relatively low charge carrier mobilities compared to their inorganic counterparts, bulk-heterojunction (BHJ) architectures are typically employed to achieve high PCEs. Although BHJ systems can indeed deliver excellent efficiencies, they may not constitute an ideal photoactive layer structure. In BHJs, the randomly intermixed donor–acceptor morphology makes it difficult to reproduce identical film structures and device efficiencies when scaling up the active area from lab-scale devices [6, 7]. In addition, BHJ morphologies are easily altered under external stress, such as continuous illumination or high-temperature exposure, often resulting in poor device stability [8–10]. Furthermore, the device optimization process is inherently complicated, as BHJ performance is strongly influenced by multiple parameters, including (1) the

donor-to-acceptor weight ratio [11], (2) the choice of host solvent and processing additives [12–15], and (3) post-treatments such as thermal or solvent-vapor annealing [16, 17]. These complex and time-consuming optimization steps pose significant challenges to further development and large-scale commercialization of OSCs.

Bilayer (or pseudo-bilayer) OSCs can overcome such limitations of BHJs, and recently they have achieved power conversion efficiencies (PCEs) comparable to those of BHJ devices, exceeding 20% [18, 19]. Bilayer structures can be realized either by using orthogonal solvents or by employing similar solvents for processing donor and acceptor materials. The former approach typically produces well-separated bilayers [20–22], whereas the latter results in an intentionally intermixed region between donor and acceptor layers within the active layer, often referred to as a pseudo-bilayer or p–i–n structure [23–25]. Notably, several studies have reported superior device stability in bilayer OSCs (including both well-separated and pseudo-bilayer structures) compared to BHJ devices [19, 26], suggesting that further systematic investigations into the stability of bilayer OSCs are highly needed.

A combination of polymer donors and NFAs is commonly used in both efficient BHJ and bilayer OSCs. Bilayer OSCs are typically fabricated using a conventional device structure (i.e., Glass/ITO/HTL/donor/acceptor/ETL/Al or Ag), where the different solubility properties of donor and acceptor materials in orthogonal solvents are strategically used to form a bilayer system [21, 22]. In this device configuration, the acceptor layer is located adjacent to the ETL and is directly involved in electron extraction. Therefore, forming a suitable surface condition and interface morphology is crucial for achieving efficient device performance, avoiding undesirable energetic mismatch or charge trapping in bilayer OSCs [20, 27]. In addition, since NFAs generally have a lower bandgap than polymer donors, the absorption range can be further tuned by introducing a third component into the acceptor layer [28]. These donor/binary acceptor systems are termed ternary bilayer OSCs, where the binary acceptor is a mixture of two acceptors. Indeed, several recent studies have introduced binary NFA systems into bilayer OSCs, demonstrating improvements in device performance and stability [19, 29–31]. However, a systematic understanding of how binary NFA systems influence bilayer OSC characteristics is still lacking. Therefore, it is important to investigate whether employing a binary NFA system is an effective strategy for enhancing the performance and stability of bilayer OSCs [32].

Herein, we investigate the effects of introducing a binary NFA system into bilayer OSCs—referred to as ternary bilayer OSCs to reflect the three-component architecture of the donor/binary acceptor—on both PCE and thermal stability. PM6 was used as the polymer donor, while IDIC and IT-4F used as the non-fullerene acceptors. We found that bilayer OSCs employing a binary IDIC:IT-4F (0.7:0.3 w/w) acceptor layer exhibit improved PCE with markedly prolonged thermal endurance, highlighting the potential of this work as a comprehensive materials engineering solution for high performance bilayer architectures. Interestingly, IDIC tends to aggregate strongly which leads to rough surface morphologies in neat films as well as bilayer films. However, this aggregation is effectively suppressed by the incorporation of IT-4F, which exhibits weaker crystallinity and forms smoother film morphologies than IDIC. The suppression of IDIC aggregation results in a more favorable interface between the acceptor and electron-transport layers, thereby improving device robustness under thermal stress with maintaining efficient charge extraction in PM6/IDIC:IT-4F bilayer OSCs. In particular, pronounced IDIC aggregation is observed in PM6/IDIC devices after thermal annealing, whereas this aggregation is dramatically suppressed in PM6/IDIC:IT-4F devices, indicating that IT-4F effectively inhibits IDIC aggregation. Furthermore, the non-radiative voltage loss is reduced in PM6/IDIC:IT-4F devices after annealing compared to PM6/IDIC devices. These results demonstrate that employing a binary NFA system is an effective strategy for simultaneously enhancing efficiency and thermal stability in bilayer OSCs, especially when the NFA exhibits a strong tendency to aggregate. While this investigation focuses on the specific IDIC:IT-4F system, this strategy suggests its potential versatility across other NFA systems susceptible to excessive aggregation [33, 34].

2 | Results and Discussion

2.1 | Characterization of Bilayer Organic Solar Cells

PM6 and IDIC were selected as donor and acceptor materials, since bilayer OSCs with these materials showed comparably high device performance with that of BHJ devices as previously reported [21, 22]. IT-4F was selected as a third component material, as we expected ITIC derivatives could show good performance in bilayer OSCs based on our previously reported study [35]. IT-4F has lower band gap energy compared to that of IDIC, which is beneficial to obtain higher photocurrents (Figure S1). Bilayer OSCs were fabricated with a conventional structure (Figure 1a). Bilayer films of D/A layers were formed using orthogonal solvents, and details can be found in the *Experimental Section*. The overall device structures and material combinations are energetically suitable, suggesting energy level mismatching cannot affect device performance (Figure 1b). It is noteworthy that IT-4F has the smallest band gap energy of about 1.56 eV, which is beneficial to obtain high photocurrents, and IDIC has slightly larger band gap energy, but shallower LUMO level is likely to obtain high open-circuit voltages.

We compared device performance measured under 1 Sun of PM6/acceptor bilayers, where acceptors are IDIC *vs.* IDIC:IT-4F (0.7:0.3 w/w) *vs.* IT-4F. Current density–voltage (*J-V*) characteristics and external quantum efficiency (EQE) spectra are shown in Figure 1c and 1d, respectively, and corresponding photovoltaic parameters are summarized in Table 1. As expected from absorption properties, PM6/IT-4F devices showed the highest short-circuit current density (J_{SC}), and PM6/IDIC devices showed the highest open-circuit voltages (V_{OC}). Interestingly, PM6/IDIC:IT-4F devices showed similarly high J_{SC} with that of PM6:IT-4F devices, and similarly high V_{OC} with that of PM6/IDIC devices, leading to the highest PCE compared to the others. We further tested bilayer OSCs with varying blend ratio of IDIC:IT-4F systematically from 1:0 to 0:1 (Figure S2 and Table S1). With increase in IT-4F ratio, J_{SC} increases and V_{OC} decreases gradually, close to those of PM6/IT-4F devices. The gradual evolution of V_{OC} can suggest an alloy-type mixed NFA phase [36–38], consistent with the intermediate π–π stacking peak position in the IDIC:IT-4F films, which will be discussed in the following section; however, detailed ternary charge generation mechanisms are beyond the scope of this work. With specific ratio

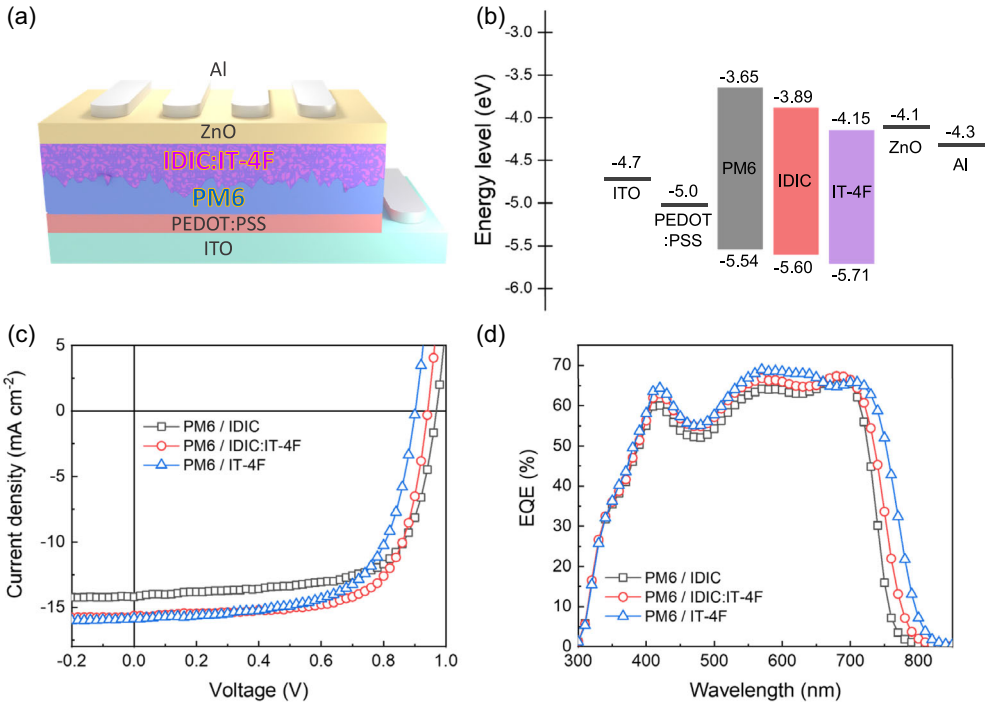

FIGURE 1 | (a) Device structure of bilayer OSCs with PM6 as donor and IDIC, IDIC:IT-4F blend and IT-4F as acceptor layer. (b) Energy band diagram of the devices. (c) *J-V* curves and (d) EQE spectra of optimum devices.

TABLE 1 | Summarized photovoltaic parameters of bilayer OSCs. (Average and standard deviation values were calculated from 10 devices as stated in parenthesis.).

Active layer	J_{SC} (mA cm^{-2})	V_{OC} (V)	FF	PCE (%)
PM6/IDIC	14.2 (14.2 ± 0.30)	0.970 (0.958 ± 0.012)	0.687 (0.655 ± 0.029)	9.34 (9.05 ± 0.21)
PM6/IDIC:IT-4F	15.6 (15.5 ± 0.20)	0.950 (0.935 ± 0.011)	0.697 (0.657 ± 0.022)	10.3 (9.71 ± 0.26)
PM6/IT-4F	15.8 (15.9 ± 0.43)	0.904 (0.884 ± 0.020)	0.648 (0.616 ± 0.018)	9.26 (8.78 ± 0.27)

of IDIC:IT-4F = 0.7:0.3, the devices showed similar J_{SC} and enhanced V_{OC}, compared to PM6/IT-4F, leading to enhanced PCEs.

We investigate light intensity-dependent photovoltaic parameters, namely J_{SC} and V_{OC}, to check whether the effect of bimolecular or trap-assistant recombination [39], respectively, is relevant to device performance or not. In terms of bimolecular recombination rate, all devices, including PM6/IDIC, PM6/IDIC:IT-4F, and PM6/IT-4F, showed similar trends of J_{SC} *vs.* light intensity characteristics (Figure S3a), indicating bimolecular recombination is not the main origin of enhanced PCEs in the binary NFA system. For V_{OC} *vs.* light intensity characteristics, which normally reflect trap-assisted recombination information, PM6/IDIC devices showed slightly lower trap-assisted recombination losses compared to the other devices of PM6/IDIC:IT-4F and PM6/IT-4F system (Figure S3b). Nevertheless, V_{OC} *vs.* light intensity characteristics is not dramatically different among all the devices. Therefore, it can be concluded that the enhanced PCEs in the binary NFA system could originate from 1) similarly high J_{SC} (close to that of PM6/IT-4F) without any influence on bimolecular recombination, and 2) middle value of V_{OC} between PM6/IDIC and PM6/IT-4F devices, with 3) maintaining fill factor. Detailed morphological characteristics and V_{OC} analysis will be discussed in following sections:

2.2 | Crystalline Structure of Neat Acceptor Films

To further identify the origin of enhanced device performance rather than deteriorated with binary NFA system, morphological properties are characterized via grazing incident wide-angle X-ray scattering (GIWAXS) and atomic force microscopy (AFM) measurements of neat NFA films. Line-cut profiles and 2D pattern images of GIWAXS measurement are shown in Figure 2a, b, respectively. To quantitatively evaluate the crystallization and stacking properties, d-spacing, and crystalline coherence length (CCL) were extracted and are summarized in Table S2. Neat IDIC film exhibited clear and strong π-π stacking peak along out-of-plane direction as well as lamellar stacking features along in-plane direction, indicative of favorable crystalline structure for efficient charge transport in OSC device architecture. For lamellar stacking along the in-plane direction (q_{xy}), neat IDIC film shows the largest CCL of 77.3 Å, reflecting a large lamellar coherent domain size, whereas neat IT-4F film showed significantly smaller CCL of 36.3 Å. Interestingly, IDIC:IT-4F binary film has almost

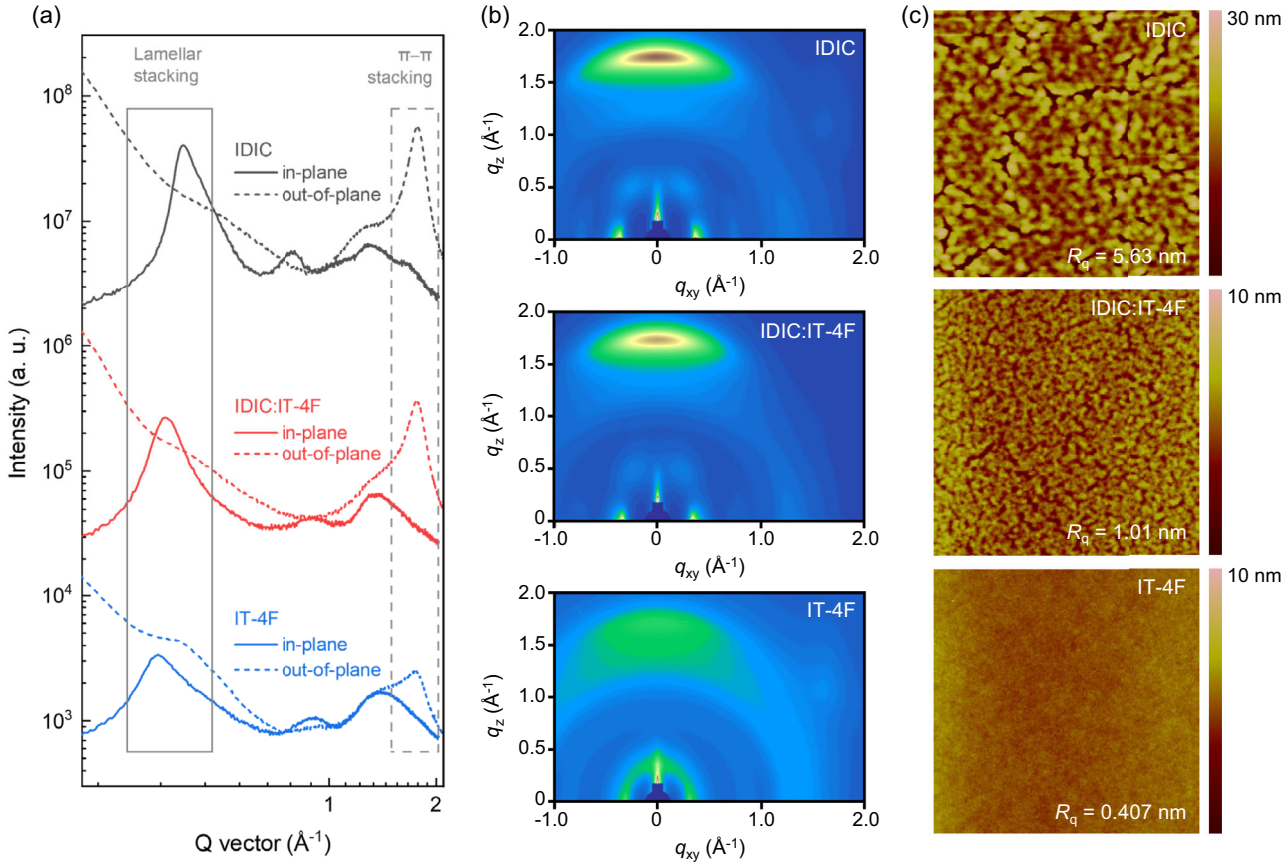

FIGURE 2 | (a) Line-cut profiles along in-plane (dashed) and out-of-plane (solid) directions and (b) pattern images of GIWAXS measurement for neat acceptor samples of IDIC, IDIC:IT-4F, and IT-4F. (c) AFM topographical images of the neat acceptor samples (image scale: 2 × 2 μm).

same π-π stacking peak (namely, clear and strong peak intensity) along out-of-plane direction with that of IDIC film, despite of blended with relatively less crystalline molecule of IT-4F. Notably, lamellar stacking peak along in-plane direction of IDIC:IT-4F binary film is located in the middle of that of IDIC and IT-4F, indicating an intermediate lamellar spacing in the intermixed acceptor phase. To identify the effect of IT-4F, we investigated the π-π stacking peak along in-plane direction of IDIC:IT-4F binary film. The CCL of IDIC:IT-4F decreases to 66.9 Å compared to neat IDIC, suggesting that IT-4F effectively suppress excessive IDIC aggregation.

Surface topological images for neat NFA films are well consistent with the GIWAXS data (Figure 2c). IDIC film showed strong aggregation morphologies with high RMS roughness of 5.63 nm. On the contrary, IT-4F film exhibited no aggregation properties with very smooth RMS roughness of 0.407 nm. IDIC:IT-4F binary film still showed aggregation features but its surface roughness was dramatically reduced to 1.01 nm (RMS roughness), compared to that of IDIC film [40, 41].

As our devices were fabricated in conventional structure, acceptor layer is contacted to electron transport layer (ETL) and top electrode. To obtain efficient bilayer OSCs, it is important to make smooth surface roughness of acceptor layer in order to minimize any losses in terms of charge extraction from photoactive layer to ETL and top electrode. At this regard, our IDIC:IT-4F binary system provide smooth surface roughness with maintaining strong π-π stacking tendency, resulting in ideal charge extraction pathways during device operation.

2.3 | Thermal Stability of Bilayer Organic Solar Cells

Due to strong aggregation of IDIC molecules, we expected that devices may not be stable under any stressed conditions such as under 1 Sun illumination or high-temperature circumstances. We investigate device stability of PM6/IDIC vs. PM6/IDIC:IT-4F vs. PM6/IT-4F bilayer OSCs to confirm whether reduced aggregation of IDIC by introducing IT-4F can help to improve device stability. Note that here we only focus on investigation of thermal stability, rather than photostability or operational ISOS test, to obtain a clear conclusion with simple stress conditions. First, bilayer OSCs were characterized with various pre-annealing condition before coating ETL and Al top electrodes: without and with pre-annealing at 120°C, 150°C, and 180°C (Figure 3a). As expected, PCEs of PM6/IDIC bilayer devices significantly decreased with above 150°C of pre-annealing condition. On the other hand, PCEs of PM6/IDIC:IT-4F and PM6/IT-4F bilayer devices were maintained regardless of pre-annealing condition compared to without pre-annealing. Note that PM6/IDIC:IT-4F devices showed slightly reduced PCEs at 180°C of pre-annealing condition, indicating IDIC aggregation still exists but IT-4F molecules seem to inhibit this aggregation. As shown in Figure S5, the distinct haze observed in PM6/IDIC films at high annealing temperatures is effectively suppressed in the binary IDIC:IT-4F system, which exhibits stable morphology regardless of thermal annealing conditions. Absorption properties also support that IDIC aggregation is effectively suppressed in the binary system. While the IDIC film shows a red-shift in its

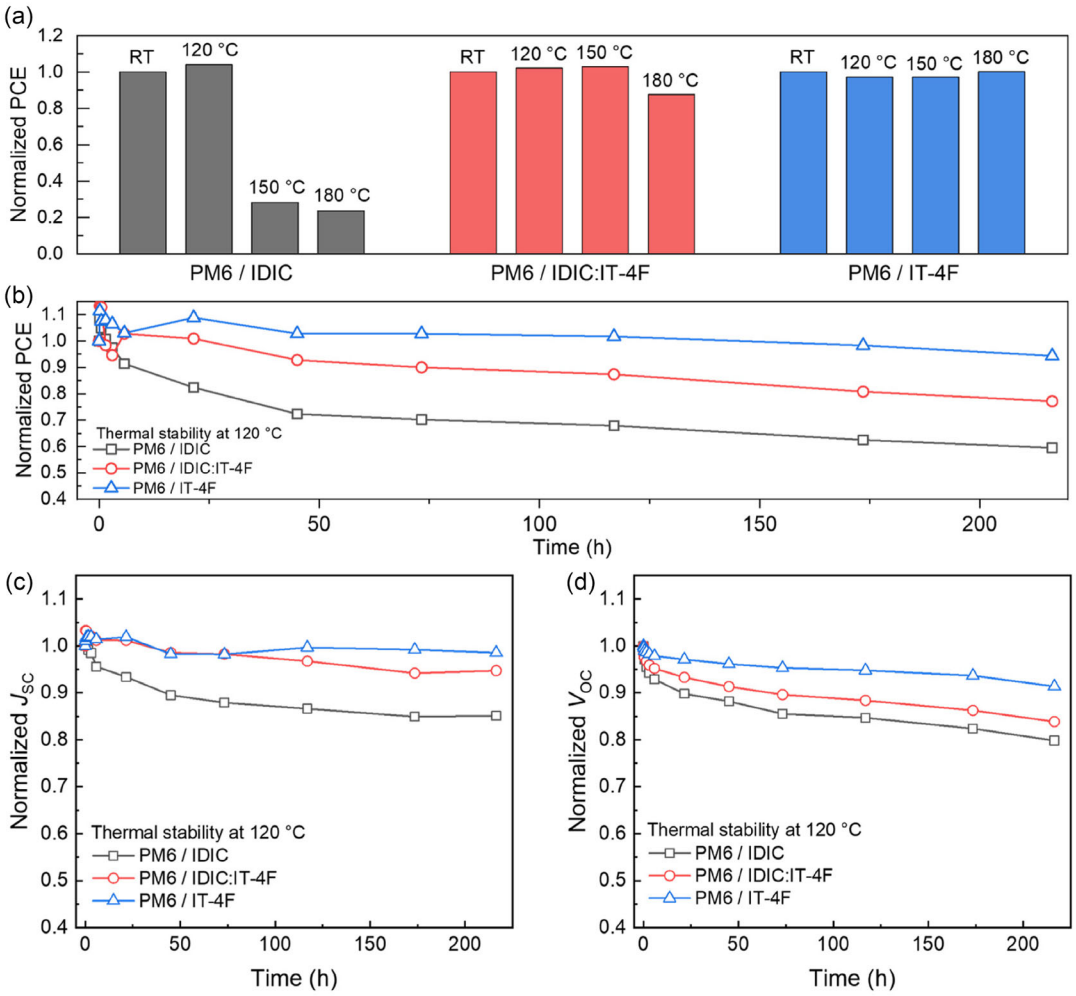

FIGURE 3 | (a) Normalized PCEs of bilayer OSCs as a function of pre-annealing temperature. Normalized (b) PCE, (c) J_{SC} and (d) V_{OC} as a function of thermal annealing time of bilayer OSCs. (Devices were continuously thermally annealed at 120°C in N_2-glove box).

absorption peak upon pre-annealing at 150°C, this shift is significantly decreased in the IDIC:IT-4F film (Figure S6).

Thermal stability was tested with continuous post-annealing of devices on a hot plate at 120°C, and corresponding normalized PCE *vs.* annealing time characteristics are shown in Figure 3b. Although PM6/IDIC devices showed maintained PCEs with pre-annealing at 120°C aforementioned, the devices were not thermally stable with post-annealing condition, showing considerably reduced PCEs. PM6/IDIC:IT-4F devices showed also slightly but less reduced PCEs compared to those of PM6/IDIC devices, whereas PM6/IT-4F devices exhibited thermally stable characteristics. PCE reduction upon thermal annealing of PM6/IDIC devices could be attributed mainly from reduction of all photovoltaic parameters, namely J_{SC}, V_{OC} and fill factor (Figure 3c,d and Figure S7, respectively). In case of PM6/IDIC:IT-4F devices, reduced PCEs upon thermal annealing could originate from mainly V_{OC}, rather than J_{SC} and fill factor which were relatively well maintained as its original values measured without thermal annealing. Maintained J_{SC} and fill factor of PM6/IDIC:IT-4F devices indicate charge generation and extraction properties seem to be rarely affected by thermal annealing, indicative of less changes in surface morphology of IDIC:IT-4F binary system upon thermal annealing which will be discussed subsequently.

2.4 | Surface Morphology and Non-Radiative Open-Circuit Voltage Loss Analyses

To identify the effect of thermal annealing to bilayer films and devices, we firstly investigate surface morphology analysis of PM6/IDIC, PM6/IDIC:IT-4F and PM6/IT-4F bilayer films using AFM measurement (Figure 4). In case of PM6/IDIC bilayer, surface morphology was significantly changed by thermal annealing; strong aggregation features appeared after thermal annealing with significant increase of RMS roughness from 1.43 to 14.8 nm, possibly due to IDIC aggregation (Figure 4d). In case of PM6/IDIC:IT-4F bilayer, surface morphology was also changed by thermal annealing with increased RMS roughness from 1.56 to 3.82 nm with partially aggregated sites, also possibly came from IDIC aggregation (Figure 4e). Less aggregation properties of PM6/IDIC:IT-4F bilayer after thermal annealing indicate IT-4F molecules inhibit IDIC aggregation well. This less change of film morphologies can provide less change in charge generation characteristics at donor/acceptor interfaces as well as charge extraction properties at acceptor/ETL, consistent with maintained J_{SC} and fill factor as discussed previously. Surface morphology of PM6/IT-4F bilayer was not affected by thermal annealing, consistent with the thermal stability result (Figure 4f).

To investigate V_{OC} reduction upon thermal annealing, we compared non-radiative V_{OC} loss (ΔV_{OC}^{nonrad}) of PM6/IDIC, PM6/

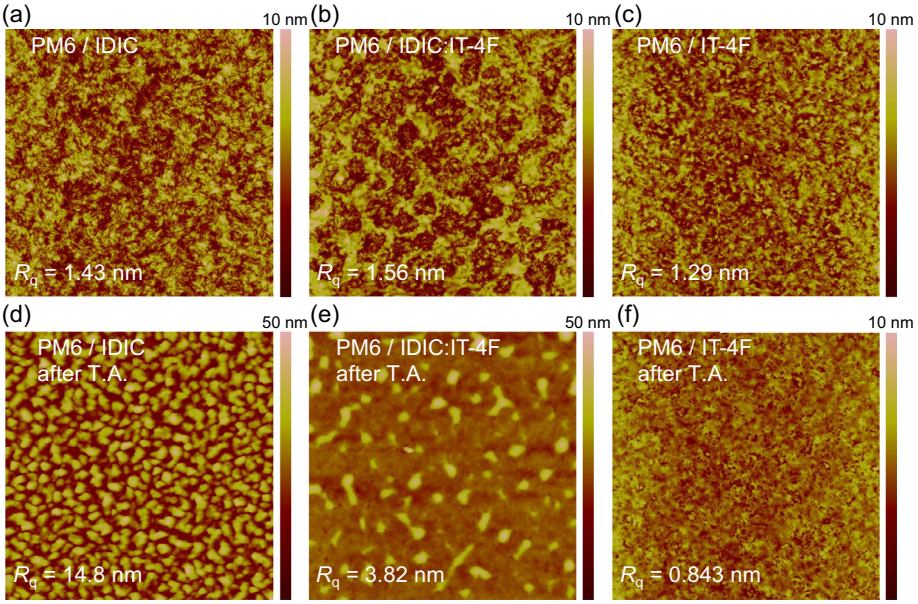

FIGURE 4 | AFM topographical images of (a,d) PM6/IDIC, (b,e) PM6/IDIC:IT-4F and (c,f) PM6/IT-4F bilayer films without and with thermal annealing at 150°C for 10 min, respectively. (Image scale: 2 × 2 μm).

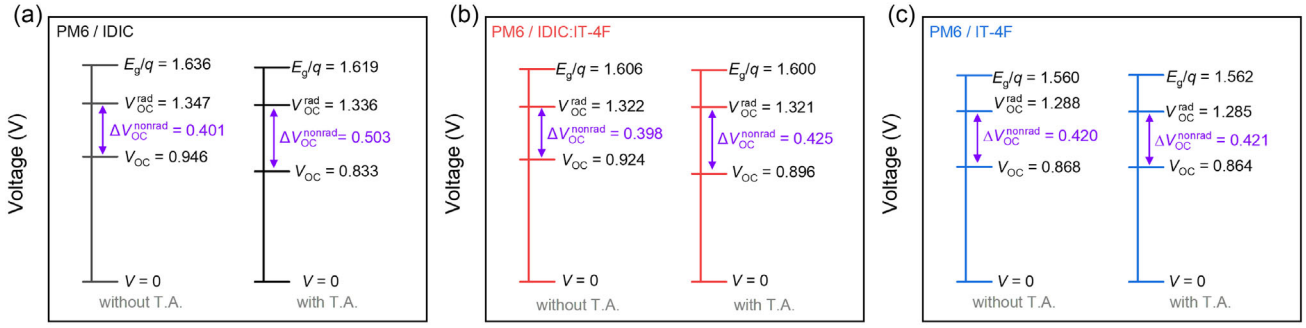

FIGURE 5 | Summarized voltage loss of (a) PM6/IDIC, (b) PM6/IDIC:IT-4F and (c) PM6/IT-4F bilayer OSCs without vs. with thermal annealing at 120°C for 5.5 h.

IDIC:IT-4F and PM6/IT-4F bilayer OSCs without *vs.* with thermal annealing at 120°C for 5.5 h, as summarized in Figure 5. Fourier-transform photocurrent spectroscopy external quantum efficiency (FTPS-EQE) and electroluminescence (EL) spectra measurements were used for this analysis, and corresponding plot details can be found in Figure S8 and Table S4. The largest ΔV_{OC}^{nonrad} increase by 102 meV and a minor increase of ΔV_{OC}^{nonrad} by 27 meV were observed after thermal annealing for PM6/IDIC and PM6/IDIC:IT-4F bilayer OSCs, respectively. PM6/IT-4F bilayer devices did not show any change of ΔV_{OC}^{nonrad}. Therefore, IT-4F molecules inhibit not only IDIC aggregation but also non-radiative V_{OC} losses in IDIC:IT-4F binary system, resulting in less deterioration of device performance upon thermal stress. Decrease of V_{OC} for PM6/IDIC:IT-4F bilayer devices upon thermal annealing (Figure 3d) was the main origin of decrease of PCE, and it is not just from increase of ΔV_{OC}^{nonrad}. Non-ideal surface morphology between PM6/IDIC:IT-4F bilayer and ETL after thermal annealing also can affect V_{OC} reduction possibly due to increase of charge trapping occurred in IDIC aggregation, etc. In addition, molecular aggregation and interfacial morphology changes can increase energetic disorder and trap density [42], and structural degradation can also promote trap-assisted non-radiative recombination and increases recombination energy losses [43, 44]. This interpretation is consistent with our experimental observation of the increased ΔV_{OC}^{nonrad} upon thermal annealing, further highlighting the critical role of interfacial disorder management in bilayer architectures [45]. Therefore, this work demonstrated a materials strategy to improve the thermal stability of bilayer architectures, showing that a binary-acceptor formulation can effectively stabilize the acceptor morphology and interface between the acceptor and ETL.

3 | Conclusion

In conclusion, we investigated the effect of introducing a binary NFA system into bilayer OSCs on device performance and thermal stability, particularly focusing on stabilizing the acceptor morphology and interfacial contact with the ETL under thermal stress. The PM6/IDIC:IT-4F bilayer OSCs exhibited the highest PCE of 10.3%, outperforming both PM6/IDIC and PM6/IT-4F devices. The strong face-on π–π stacking orientation and the smooth surface morphology of the IDIC:IT-4F layer, enabled by suppressed IDIC aggregation, provided an ideal interface between the acceptor layer and the

ETL, leading to enhanced device performance. Thermal stability studies further revealed that the PM6/IDIC:IT-4F devices exhibited superior durability to thermal stress compared to PM6/IDIC devices, mainly due to reduced IDIC aggregation and suppressed non-radiative voltage loss. Overall, these results demonstrate that introducing a binary NFA system is an effective strategy to simultaneously improve both efficiency and thermal stability in bilayer OSCs, highlighting the importance of suppressing aggregation in the top acceptor layer to realize highly efficient and stable photovoltaic devices.

4 | Experimental Section

4.1 | General

UV–vis spectrometry was performed using a Varian Carry 5000 spectrophotometer. AFM images were obtained using a Veeco AFM microscope in tapping mode. Grazing incidence wide-angle X-ray scattering (GI-WAXS) measurements were carried out at the PLS-II 9A U-SAXS beam line of Pohang Accelerator Laboratory, Republic of Korea. PM6, IDIC, and IT-4F were purchased from 1-Material. Chlorobenzene and dichloromethane were purchased from Sigma Aldrich.

4.2 | Device Fabrication Procedures and Characterization

Pre-patterned ITO on glass substrates were sequentially cleaned by ultrasonication with distilled water, acetone, and isopropanol. PEDOT:PSS (AI4083) was spin-coated onto the ITO substrate and annealed at 150 °C for 10 min. For bilayer devices, PM6 was dissolved in chlorobenzene (CB):1,8-octanedithol (ODT) (100:1 vol ratio) with a concentration of 10 mg mL^{-1} at 100 °C. IDIC, IDIC:IT-4F (0.7:0.3, w/w), IT-4F were dissolved in dichloromethane (DCM) with a concentration of 6.5 mg mL^{-1} at the room temperature. PM6 solutions were spin-cast on top of the PEDOT:PSS layer and thermal annealed at 100 °C for 5 min in an N_2-filled glove box. Then, the acceptor layer was spin-coated on top of PM6 layer, and the ZnO layer was spin-coated, sequentially. To deposit Al (100 nm) electrodes by thermal evaporation, a vacuum chamber was pumped down under $\sim 10^{-7}$ Torr. The area of the Al electrode defined an active area of 13 mm^2. *J-V* characteristics were collected with a Keithley 2635 A source measurement unit inside the N_2-filled glove box using a high quality optical fiber to guide the light from a solar simulator to the device. For thermal stability, the devices were aged at 120°C inside the N_2-filled glove box. *J–V* characteristics were measured at specified intervals using the solar simulator, rather than through simultaneous measurement during thermal stress. Light intensities were modulated with neutral density filters to measure the light intensity dependent photovoltaic parameters. External quantum efficiency (EQE) measurements were performed using a PV measurement QE system using monochromatic light from a xenon lamp under ambient conditions. The monochromatic light was chopped at 100 Hz and the device was measured relative to a standard Si photodiode using a lock-in-amplifier.

4.3 | Voltage Loss Analysis

FTPS was recorded using an in-house built FTPS setup, which consisted of an INVENIO-R Fourier-transform infrared (FTIR) spectrometer from Bruker, equipped with a tungsten-halogen lamp and quartz beam splitter. The SR570 low-noise preamplifier from Stanford Research Systems was used to amplify the photocurrent signal from solar cells and it was fed back into the external detector port of the FTIR system. EL spectrum was measured using the QEPRO-VIS-NIR spectrophotometer with an integral sphere from Ocean Optics. The integral sphere and spectrophotometer were calibrated to measure absolute irradiance by using an HL-3-plus-INT-CAL light source from Ocean Optics, and EQEEL was calculated with the injected current versus EL spectrum unit of absolute irradiance. The injected current was recorded using KEITHLEY 2401 source meter.

Acknowledgements

This research was supported by the Pukyong National University Industry-university Cooperation Foundation's 2024 (202408160001). This work was supported by the National Research Foundation of Korea (NRF) grant funded by the Korea government (MSIT) (NRF-2025-00512708).

Funding

Pukyong National University Industry-university Cooperation Foundation's 2024 (202408160001), National Research Foundation of Korea (NRF-2025-00512708).

Conflicts of Interest

The authors declare no conflicts of interest.

Data Availability Statement

The data that support the findings of this study are available in the supplementary material of this article.

References

1. L. Zhu, M. Zhang, G. Zhou, et al., "Achieving 20.8% Organic Solar Cells via Additive-Assisted Layer-by-Layer Fabrication with Bulk p-i-n Structure and Improved Optical Management," *Joule* 8 (2024): 3153. https://doi.org/10.1016/j.joule.2024.08.001.

2. K. Yin, Y. Li, X. Li, et al., "Realizing Over 20% Efficiency in Nonhalogenated Solvent-Processed Organic Solar Cells Via Linking Site Engineering of Giant Molecule Acceptors," *ACS Energy Letters* 10 (2025): 6004. https://doi.org/10.1021/acsenergylett.5c02742.

3. J. Zhang, X. Duan, X. Li, et al., "Achieving 20% Efficiency in Binary Organic Solar Cells with Suppressed Non-Radiative Recombination *via* Triphenylamine Halides," *Energy Environmental Science* 18 (2025): 5378. https://doi.org/10.1039/D5EE01165E.

4. M. Kaltenbrunner, M. S. White, E. D. Głowacki, et al., "Ultrathin and Lightweight Organic Solar Cells with High Flexibility," *Nature Communications* 3 (2012): 770. https://doi.org/10.1038/ncomms1772.

5. F. Yang, Y. Huang, Y. Li, and Y. Li, "Large-Area Flexible Organic Solar Cells," *Npj Flexible Electronics* 5 (2021): 30. https://doi.org/10.1038/s41528-021-00128-6.

6. R. Basu, F. Gumpert, J. Lohbreier, et al., "Large-Area Organic Photovoltaic Modules with 14.5% Certified World Record Efficiency," *Joule* 8 (2024): 970. https://doi.org/10.1016/j.joule.2024.02.016.

7. X. Liu, Y. Zhang, S. Fu, et al., "In-Depth Investigation of Morphology Evolution in Highly Efficient Pseudo-Planar Heterojunction All-polymer Organic Photovoltaics," *Advance Functional Materials* 35 (2025): 2500975. https://doi.org/10.1002/adfm.202500975.

8. Z. Suo, X. Si, W. Zhao, et al., "Enhancing the Thermal Stability of Organic Solar Cells by Locking Morphology with Ethyl Cellulose Additive," *Solar RRL* 9 (2025): 2400927. https://doi.org/10.1002/solr.202400927.

9. W. Yang, Z. Luo, R. Sun, et al., "Simultaneous Enhanced Efficiency and Thermal Stability in Organic Solar Cells from a Polymer Acceptor Additive," *Nature Communications* 11 (2020): 1218. https://doi.org/10.1038/s41467-020-14926-5.

10. H. Zhao, N. Prine, S. Kundu, G. Ma, and X. Gu, "Effect of Thermal Stress on Morphology in High-Performance Organic Photovoltaic Blends," *JACS Au* 4 (2024): 4334. https://doi.org/10.1021/jacsau.4c00631.

11. N. G. An, J. Y. Kim, and D. Vak, "Machine Learning-Assisted Development of Organic Photovoltaics *via* High-Throughput *In Situ* Formulation," *Energy Environmental Science* 14 (2021): 3438. https://doi.org/10.1039/D1EE00641J.

12. T. H. Lee, S. Y. Park, B. Walker, et al., "A Universal Processing Additive for High-Performance Polymer Solar Cells," *RSC Advances* 7 (2017): 7476. https://doi.org/10.1039/C6RA27944A.

13. B. Guo, J. Li, K. Xiang, et al., "Isopropanol: A Green Solvent Additive for 20% Efficiency Organic Solar Cells with Excellent Generality and Improved Eco-Compatibility," *Advance Functional Materials* 36 (2025): e18732. https://doi.org/10.1002/adfm.202518732.

14. Z. Zheng, E. He, J. Wang, et al., "Revealing the Role of Solvent Additives in Morphology and Energy Loss in Benzodifuran Polymer-Based Non-Fullerene Organic Solar Cells," *Journal of Materials Chemistry A* 9 (2021): 26105. https://doi.org/10.1039/D1TA08893A.

15. H. Wang, Z. He, X. Liu, et al., "Temporally Stepwise Crystallization via Dual-Additive Orchestration: Resolving the Crystallinity-Domain Size Paradox for High-Efficiency Organic Photovoltaics," *Journal of Energy Chemistry* 112 (2026): 370. https://doi.org/10.1016/j.jechem.2025.08.059.

16. B. Walker, D. Han, M. Moon, et al., "Effect of Heterocyclic Anchoring Sequence on the Properties of Dithienogermole-Based Solar Cells," *ACS Applied Materials Interfaces* 9 (2017): 7091. https://doi.org/10.1021/acsami.6b14804.

17. C. L. Radford, R. D. Pettipas, and T. L. Kelly, "Watching Paint Dry: Operando Solvent Vapor Annealing of Organic Solar Cells," *Journal of Physical Chemistry Letters* 11 (2020): 6450. https://doi.org/10.1021/acs.jpclett.0c01934.

18. L. Tan, Z. Zhao, S. Chung, et al., "Suppressing Nongeminate Charge Recombination Triggers 19.5% Efficiency Bilayer Organic Solar Cells," *ACS Materials Letters* 7 (2025): 376. https://doi.org/10.1021/acsmaterialslett.4c02181.

19. X. Lai, H. Lai, M. Du, et al., "Bilayer Quasiplanar Heterojunction Organic Solar Cells with a Co-Acceptor: A Synergistic Approach for Stability and Efficiency," *Chemistry of Materials* 34 (2022): 7886. https://doi.org/10.1021/acs.chemmater.2c01604.

20. S. Y. Park, C. Labanti, J. Luke, Y.-C. Chin, and J.-S. Kim, "Organic Bilayer Photovoltaics for Efficient Indoor Light Harvesting," *Advanced Energy Materials* 12 (2022): 2103237. https://doi.org/10.1002/aenm.202103237.

21. S. Y. Park, S. Chandrabose, M. B. Price, et al., "Photophysical Pathways in Efficient Bilayer Organic Solar Cells: The Importance of Interlayer Energy Transfer," *Nano Energy* 84 (2021): 105924. https://doi.org/10.1016/j.nanoen.2021.105924.

22. T. H. Lee, S. Y. Park, W.-W. Park, et al., "Efficient Exciton Diffusion in Organic Bilayer Heterojunctions with Nonfullerene Small Molecular Acceptors," *ACS Energy Letters* 5 (2020): 1628. https://doi.org/10.1021/acsenergylett.0c00564.

23. K. Jiang, J. Zhang, Z. Peng, et al., "Pseudo-Bilayer Architecture Enables High-Performance Organic Solar Cells with Enhanced Exciton Diffusion Length," *Nature Communications* 12 (2021): 468. https://doi.org/10.1038/s41467-020-20791-z.

24. Y. Yan, X. Zhou, F. Zhang, et al., "High-Performance Pseudo-Bilayer Ternary Organic Solar Cells with PC_{71} BM as the Third Component," *Journal of Materials Chemistry A* 10 (2022): 23124. https://doi.org/10.1039/D2TA04784E.

25. Y. Xie, K. Wang, H. Yu, et al., "Improving the Efficiency of Layer-by-Layer Organic Photovoltaics to Exceed 19% by Establishing Effective Donor–Acceptor Interfacial Molecular Interactions," *ACS Applied Materials Interfaces* 17 (2025): 15741. https://doi.org/10.1021/acsami.5c01195.

26. T. Kumari, I. Vyalih, M. Á. León Luna, et al., "Bilayer Layer-by-Layer Structures for Enhanced Efficiency and Stability of Organic Photovoltaics beyond Bulk Heterojunctions," *Cell Reports Physical Science* 5 (2024): 102027. https://doi.org/10.1016/j.xcrp.2024.102027.

27. J. Luke, L. Corrêa, J. Rodrigues, et al., "A Commercial Benchmark: Light-Soaking Free, Fully Scalable, Large-Area Organic Solar Cells for Low-Light Applications," *Advanced Energy Materials* 11 (2021): 2003405. https://doi.org/10.1002/aenm.202003405.

28. N. Y. Doumon, L. Yang, and F. Rosei, "Ternary Organic Solar Cells: A Review of the Role of the Third Element," *Nano Energy* 94 (2022): 106915. https://doi.org/10.1016/j.nanoen.2021.106915.

29. L. Zhan, S. Li, X. Xia, et al., "Layer-by-Layer Processed Ternary Organic Photovoltaics with Efficiency over 18%," *Advanced Materials* 33 (2021): 2007231. https://doi.org/10.1002/adma.202007231.

30. M. Ren, G. Zhang, Z. Chen, et al., "High-Performance Ternary Organic Solar Cells with Controllable Morphology via Sequential Layer-by-Layer Deposition," *ACS Applied Materials Interfaces* 12 (2020): 13077. https://doi.org/10.1021/acsami.9b23011.

31. J. Wan, L. Zhang, Q. He, et al., "High-Performance Pseudoplanar Heterojunction Ternary Organic Solar Cells with Nonfullerene Alloyed Acceptor," *Advanced Functional Materials* 30 (2020): 1909760. https://doi.org/10.1002/adfm.201909760.

32. S. Karuthedath, Y. Firdaus, A. D. Scaccabarozzi, et al., "Trace Solvent Additives Enhance Charge Generation in Layer-by-Layer Coated Organic Solar Cells," *Small Structure* 3 (2022): 2100199. https://doi.org/10.1002/sstr.202100199.

33. Y. Chen, L. Hu, N. Chen, et al., "Boosting Efficiency of Non-Fullerene Organic Solar Cells Via Introducing Multidimensional Second Acceptors," *Solar RRL* 6 (2022): 2200302. https://doi.org/10.1002/solr.202200302.

34. Y. Zhu, A. Gadisa, Z. Peng, et al., "Rational Strategy to Stabilize an Unstable High-Efficiency Binary Nonfullerene Organic Solar Cells with a Third Component," *Advanced Energy Materials* 9 (2019): 1900376. https://doi.org/10.1002/aenm.201900376.

35. T. H. Lee, S. Y. Park, X. Du, et al., "Effects on Photovoltaic Characteristics by Organic Bilayer- and Bulk-Heterojunctions: Energy Losses, Carrier Recombination and Generation," *ACS Applied Materials Interfaces* 12 (2020): 55945. https://doi.org/10.1021/acsami.0c16854.

36. J. Zhang, Y. Zhang, J. Fang, et al., "Conjugated Polymer–Small Molecule Alloy Leads to High Efficient Ternary Organic Solar Cells," *Journal of the American Chemical Society* 137 (2015): 8176. https://doi.org/10.1021/jacs.5b03449.

37. H. Wang, Z. Zhang, X. Liu, et al., "14.55% Efficiency PBDB-T Ternary Organic Solar Cells Enabled by Two Alloy-Forming Acceptors Featuring Distinct Structural Orders," *Chemical Engineering Journal* 413 (2021): 127444. https://doi.org/10.1016/j.cej.2020.127444.

38. Y. Chen, P. Ye, Z.-G. Zhu, et al., "Achieving High-Performance Ternary Organic Solar Cells through Tuning Acceptor Alloy," *Advanced Materials* 29 (2017): 1603154. https://doi.org/10.1002/adma.201603154.

39. A. K. K. Kyaw, D. H. Wang, V. Gupta, et al., "Intensity Dependence of Current–Voltage Characteristics and Recombination in High-Efficiency

Solution-Processed Small-Molecule Solar Cells," *ACS Nano* 7 (2013): 4569. https://doi.org/10.1021/nn401267s.

40. X. Liu, Z. He, H. Wang, et al., "Unraveling Cross-Scale Fluorination Mechanisms in Non-Fullerene Acceptors for High-Efficiency Organic Photovoltaics," *Advanced Functional Materials* 36 (2026): e17542. https://doi.org/10.1002/adfm.202517542.

41. Y. Zhang, Y. Zhang, X. Liu, et al., "Controlling the Third Component Distribution Toward High-Efficient Ternary Organic Solar Cells," *Advanced Energy Materials* 15 (2025): 2406136. https://doi.org/10.1002/aenm.202406136.

42. S. Gao, Y. Zhang, S. Jeong, et al., "Ameliorated Trap Density and Energetic Disorder *via* a Strengthened Intermolecular Interaction Strategy to Construct Efficient Non-Halogenated Organic Solar Cells," *Energy Environmental Science* 17 (2024): 5542. https://doi.org/10.1039/D4EE00291A.

43. S. Alam, H. Aldosari, C. E. Petoukhoff, et al., "Thermally-Induced Degradation in PM6:Y6-Based Bulk Heterojunction Organic Solar Cells," *Advanced Functional Materials* 34 (2024): 2308076. https://doi.org/10.1002/adfm.202308076.

44. Z.-H. Chen, P.-Q. Bi, X.-Y. Yang, et al., "Quantitatively Characterized Crystallization Effect on Recombination Energy Loss in Non-Fullerene Organic Solar Cells," *The Journal of Physical Chemistry C* 123 (2019): 12676. https://doi.org/10.1021/acs.jpcc.9b03572.

45. R. Wang, L. Han, N. Li, et al., "Reducing Voltage Losses in Organic Photovoltaics Requires Interfacial Disorder Management," *Advanced Energy Materials* 14 (2024): 2400609. https://doi.org/10.1002/aenm.202400609.

Supporting Information

Additional supporting information can be found on online in the supporting information section. **Supporting Fig. S1**: Normalized absorbance of IDIC, IDIC:IT-4F (7:3) and IT-4F neat films. **Supporting Fig. S2**: (a) *J-V* curves and (b) EQE spectra of PM6/Acceptor bilayer OSCs with various IDIC : IT-4F blend ratio from 1 : 0 to 0 : 1. **Supporting Fig. S3**: Light intensity dependent on (a) J_{SC} and (b) V_{OC} characteristics of bilayer OSCs. **Supporting Fig. S4**: (a) Ultraviolet photoelectron spectroscopy (UPS) spectra of neat acceptor films. (b) Magnified spectra of low binding energy (Fermi edge) region. **Supporting Fig. S5**: Photographs of bilayer devices with different pre-annealing temperatures. Active layer was annealed for 10 min for 120, 150 and 180°C, then ZnO and Al layers were deposited subsequently. **Supporting Fig. S6**: Normalized absorption spectra of pristine acceptor films (dashed), bilayer films before (solid) and after (short dashed) thermal annealing at 150°C for 10 min of (a) IDIC, (b) IDIC:IT-4F and (c) IT-4F samples. **Supporting Fig. S7**: Normalized fill factor measured during thermal stability test at 120°C in N_2-glove box. **Supporting Fig. S8**: Semi-logarithmic plots of measured EQE (blue solid line), FTPS-EQE (red open circle), normalized EL emission (orange solid line) and $\varphi_{EL}/\varphi_{bb}$ fitting (black solid line) as function of energy for PM6/Acceptor bilayers (a-c) without and (d-f) with thermal annealing at 120°C for 5.5 hr. **Supporting Fig. S9**: Estimated bandgap (E_g) of bilayer OSCs (a-c) with and (d-f) without thermal annealing at 120°C for 5.5 h with the method of $(E*EQE)^2$. **Supporting Fig. S10**: (a) *J-V* curves and (b) EQE spectra of bilayer OSCs without (solid) and with (dashed) thermal annealing. (The substrates were thermally annealed at 120°C for 5.5 h before coating ZnO ETL.) These device results were used for energy loss analysis (Table S3). **Supporting Table S1**: Summary of photovoltaic parameters with various IDIC : IT-4F ratio. **Supporting Table S2**: Summary of molecular packing parameters obtained from GIWAXS analysis on different acceptors. **Supporting Table S3**: Summary of energy levels measured by UPS spectra of acceptors. LUMO levels were calculated from HOMO + $E_{g,opt}$, where $E_{g,opt}$ is optical bandgap calculated from the absorption spectra. **Supporting Table S4**: Summary of voltage loss parameters. E_g and V_{OC} values from Figure S9 and S10, respectively. **Supporting Table S5**: Summary of photovoltaic parameters of bilayer OSCs with comparing thermal annealing effect (corresponding to Figure S10).